

Source detection at 100 meter standoff with a time-encoded imaging system

J. Brennan^a, E. Brubaker^a, M. Gerling^a, P. Marleau^a, M. Monterial^{a,b}, A. Nowack^{a,1}, P. Schuster^{a,2}, B. Sturm^a, M. Sweany^{a,*}

^aSandia National Laboratory, Livermore, CA 94550, USA

^bUniversity of Michigan, Ann Arbor, MI

Abstract

We present the design, characterization, and testing of a laboratory prototype radiological search and localization system. The system, based on time-encoded imaging, uses the attenuation signature of neutrons in time, induced by the geometrical layout and motion of the system. We have demonstrated the ability to detect a ~ 1 mCi ^{252}Cf radiological source at 100 m standoff with 90% detection efficiency and 10% false positives against background in 12 min. This same detection efficiency is met at 15 s for a 40 m standoff, and 1.2 s for a 20 m standoff.

Keywords:

fast neutron imaging, time-encoded imaging, radiological search instrument

1. Introduction

The detection and localization of radiological sources in various environments is an important nuclear security capability. Some scenarios require quick localization of sources in highly cluttered background environments, and others may demand detection of sources over large areas. Because of their relatively low and isotropic natural background, ability to penetrate shielding, and long attenuation length in air (approximately 100 m at fission energies), fast neutrons are a strong candidate signature of illicit nuclear material. However, despite the relatively low background flux, variability caused by environmental factors such as weather conditions (pressure and humidity), geographic location (geomagnetic rigidity), local scattering sources, and even solar cycle, lead to a systematic uncertainty in the absolute neutron background rate [1, 2]. For example, the dominant factor in the time variation for a fixed location is the solar cycle, causing a 30% variation [3]. This variability ultimately limits the detection sensitivity of gross counting detectors.

Neutron imaging can reduce susceptibility to background variability, but in the case of double scatter imagers [4] the efficiency is low, and coded-aperture imagers [5] have a limited field of view and poor imag-

ing signal to background. Both systems typically involve large numbers of detector/electronics channels that could impede fieldability and introduce systematic variability due to, for example, differences in photodetector gain and overall detector light collection efficiency. While gain variation and light collection efficiency in these systems can be calibrated to reduce systematic variability, the large number of channels adds a time and labor intensive calibration step in any measurement.

The time-encoded imaging (TEI) system described in this paper, however, has a 360-degree field of view, low channel count leading to reduced susceptibility to systematics, and does not require double scatters for localization, resulting in improved efficiency. Recently, we reported on a two-dimensional fast neutron imager using time-encoded imaging (2D-TEI) [6]. That system was designed as a proof of principle for an alternative to coded-aperture imaging, with the distinction that, rather than modulating the radiation field in space and recording the modulation with position sensitive detectors, the field was modulated in time and recorded with a time sensitive detector. The main systematic effects for such a system are those that induce a time modulation with the same rotational period as the detector rotation, of which there are few. Presented here is another system based on the TEI concept; targeting the application of radiological search at large standoff as opposed to high-resolution imaging yields a distinct detector sys-

*Corresponding author: msweany@sandia.gov

¹Currently at the University of Tennessee at Knoxville

²Currently at the University of Michigan

tem, which we call 1D-TEI. Most notably, the system uses large detector cells to increase sensitivity; the signal is modulated in only one dimension, providing localization in azimuth for sources near the horizon; and the modulation is accomplished by the detectors themselves, rather than by a separate mask, to reduce inactive detector mass.

Here we report on the performance of a 1D-TEI system for source detection at large standoff. Although our system is capable of detecting both neutron and gamma sources, we have designed it for neutron detection because neutron backgrounds are more reliably isotropic. The system design and detector response are described in Sections 2 and 3, data analysis is presented in Section 4, and measurement results for sources at several different stand-off distances are presented in Section 5.

2. Time-encoded neutron imaging system

The 1D-TEI system consists of four neutron detector cells arranged in a diamond pattern that rotate around a common vertical axis. Several different arrangements of four detector cells were studied [7], and this one was found to be optimal for source detection. As the system is rotated, the amount of shielding between each cell and a given radiological source location varies, modulating the fast neutron detection rate as a function of time. The cell configuration is shown in Fig. 1. Liquid scintillator EJ-309 was used as a detection medium for its pulse shape discrimination (PSD) capabilities, safety benefits, and neutron attenuation properties. The relevant design considerations were modulation and detection efficiency of fast neutrons. Considering modulation alone, larger detector cells are preferred for greater neutron attenuation, but pulse shape discrimination and therefore neutron detection efficiency is degraded with detector size due to decreased light collection efficiency and increased spread in their time of arrival. We studied several configurations, detailed in [8], and found that 12 in dia. \times 15 in right cylindrical cells have acceptable PSD when read out by four 5-inch Hamamatsu H6527 photomultiplier tubes. The liquid scintillator cells share an expansion reservoir with Argon gas overpressure and room to expand and contract within an estimated 80° F temperature swing. A picture of the 1D-TEI instrument is shown in Fig. 2.

The liquid scintillator cells and electronics are all affixed to a turntable that is rotated by an Arcus stepper motor. The motor is connected to a toothed wheel, and a flywheel holds a geared belt against the inside bearing of the turntable which is also toothed: this ensures constant contact and prevents slipping. A rotary encoder

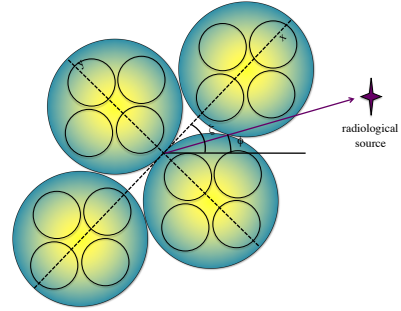


Figure 1: A rendering of the one-dimensional time-encoded imaging system (1D-TEI). As the system is rotated by angle ζ , radiation from the source, located at ϕ , is modulated by each of the detectors. The PMT layout within the detector cells is indicated by the open black circles.

is attached to the turntable ring to measure the angle of rotation. A metal divot attached to the turntable passes over a switch on the stationary mask frame to mark the end of one rotation. During measurements, an Arcus controller board reads the encoder value, motor pulse value, and the state of the frame switch, which is written to hard disk once per rotation. The 16 PMTs are read out by a Struck 3316 250 MHz desktop digitizer. Each detector is independently and asynchronously triggered and read out by applying a threshold on the sum of the four PMT digital signals. In order to achieve continuous data acquisition, the data from the Arcus controller board and the Struck digitizer are read out by separate threads. The Struck digitizer has its own clock unit for recording time-stamps, but the Arcus controller relies on the acquisition computer CPU clock. The CPU clock and the Struck digitizer clock unit are synchronized at the beginning of the acquisition by simultaneously resetting the clock unit on the digitizer while sampling the CPU clock. We expect that any delay in executing these commands is on the order of milliseconds or less and thus inconsequential compared to the typical rotation rate of 0.5 rpm.

The amount of data from the Arcus-controlled board is relatively small and can be written to disk without any appreciable delay in acquisition. The digitizer is read out whenever one of its two memory banks becomes full, at which point the acquisition switches to the other memory bank. If the data from the first bank can be downloaded to the acquisition computer and written to disk before the second memory bank fills up then the acquisition can continue without interruption. The system can handle trigger rates of up to 360 kHz, after which events are lost. The event rates for the data presented



Figure 2: Photo of the 1D-TEI instrument. The white-painted cells each contain ~ 27 L of EJ-309 liquid scintillator, and the aluminum cylinders house four PMTs for each cell. The cells are arranged in a diamond pattern on a rotational table, which is driven by a stepper motor.

here are all at least an order of magnitude below this level.

3. Detector Response

There are three aspects of the detector response that must be calibrated to determine the neutron rate as a function of time. First, a relative gain correction is necessary to combine the measurements for all PMTs on one cell to ensure azimuthal symmetry of the cell's response. However, a precise absolute energy calibration for each cell is not required. This is because the detection algorithm described below is robust against differences in efficiency between cells: it is the relative change in rate over time within each cell, due to the attenuation signature, that is critical to the detection algorithm. Second, the pulse-shape discrimination must be characterized for each cell in order to distinguish gamma interactions from neutron interactions. Finally, the timing of each deposition must be correlated correctly with the rotational position of the turntable.

3.1. Energy

In order to equalize the relative response of the four detectors, we first gain-match the four individual photomultipliers in each detector. This is accomplished by matching the normalized pulse-height spectrum resulting from a ^{22}Na gamma-ray source, centered below the

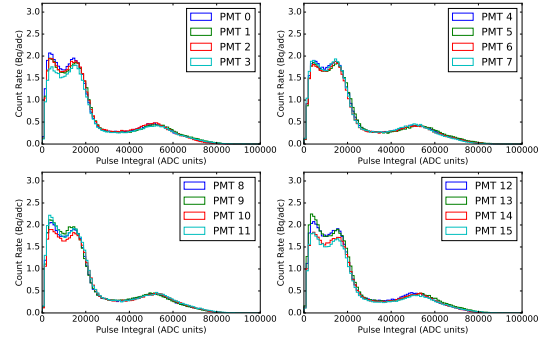


Figure 3: The energy distribution resulting from a ^{22}Na source for all 16 PMTs in the system.

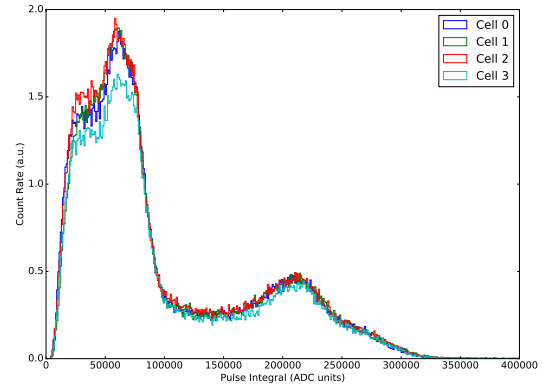


Figure 4: The summed energy distribution resulting from a ^{22}Na source for the four cells.

cell so that it is equidistant from each PMT. Figure 3 shows the distributions of the pulse integrals for all 16 PMTs in the system, indicating good overall agreement in both gain and efficiency. The Compton edge from the 1270 keV emission from ^{22}Na is visible for all distributions between 50k and 60k ADC units, and the Compton edge from the 511 keV positron annihilation gammas is visible between 10k and 20k ADC units.

Next, we reject events driven by spurious signals in one channel by adding a requirement that all four PMTs individually exceed a noise threshold. Using this selection, the integral of the sum of the four pulses is plotted in Fig. 4. Again, good overall agreement in gain is indicated by the alignment of the Compton features for each cell. Agreement in efficiency is indicated by similar event rates shown on the y-axis, with one cell slightly lower in rate than the other three: the total integrated event rates are within 10% of each other, and the greatest difference is at lower energies. As stated above, the detection algorithm is robust against small differences in efficiency from cell to cell.

Because this system depends on the modulation in rate as a function of rotation angle, it is necessary to confirm that there are no variations in efficiency or gain that are caused by factors other than the expected source attenuation. This was previously demonstrated for a similar photo-detector layout in the same size cell [8] by comparing the sum of photo-detector pulse heights from a ^{137}Cs source placed at the same height but different azimuthal angles around the cell. No discernible difference was observed. A difference in the response with height along the cell was observed, as expected due to the decrease in light collection as the average deposition height moves away from the PMT faces, however this does not affect the modulation of detection as a function of rotation angle.

3.2. Pulse-shape discrimination

In order to discriminate between gamma and neutron depositions, we define a PSD parameter on the signal from each PMT as the ratio of the tail integral of the pulse to a fixed total integral. The tail window was chosen to maximize the separation of the neutron and gamma distributions by optimizing a figure-of-merit (FOM), defined by:

$$\text{FOM} = \frac{|\mu_n - \mu_\gamma|}{\Gamma_n + \Gamma_\gamma}, \quad (1)$$

where $\mu_{n,\gamma}$ is the mean of the neutron, gamma distributions and $\Gamma_{n,\gamma}$ is the width (FWHM). The FOM is optimized for each cell, using the average PSD of the four PMTs vs. the summed pulse integral. The tail and total windows, determined in reference to the trigger time of each pulse, are indicated in Fig. 5 for one of the cells. A baseline window is defined from 0 to 48 ns.

For the final event selection, we use a Bayesian approach to pulse-shape discrimination, similar to the method outlined in [9]. Rather than averaging the PSD parameter values, the Bayesian probabilities determined for each of the four PMTs are combined to produce one overall probability for the cell. This was demonstrated in [9] to improve neutron/gamma discrimination compared to applying a decision boundary. First, the PSD parameter distribution for each PMT is fit by a double Gaussian distribution in slices of energy E over the entire energy range. For a given slice:

$$f(x, E) = \frac{1}{\sqrt{2\pi}} \left(\frac{A_\gamma(E)}{\sigma_\gamma(E)} e^{-\frac{(x-\mu_\gamma(E))^2}{2\sigma_\gamma(E)^2}} + \frac{A_n(E)}{\sigma_n(E)} e^{-\frac{(x-\mu_n(E))^2}{2\sigma_n(E)^2}} \right). \quad (2)$$

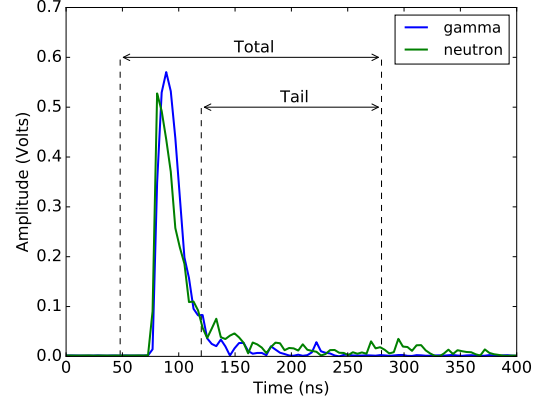


Figure 5: An example neutron (green) and gamma (blue) pulse, with the gate lengths specified for the tail and total integrals. The gates are determined by the trigger time of each pulse. A window from 0 to 48 ns is used to determine the baseline.

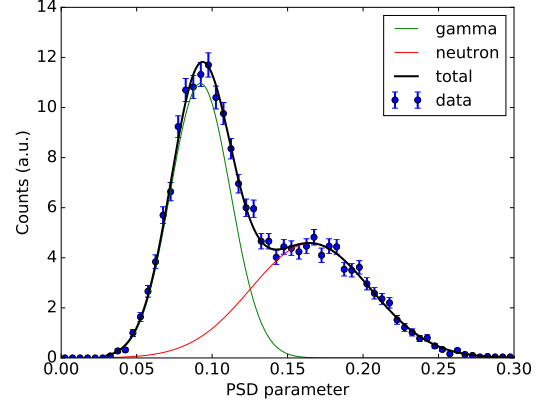


Figure 6: The PSD distribution from cell 0, PMT 0 for an amplitude slice of 43099-43452 ADC counts, in which the contribution from the gamma (green) and neutron (red) Gaussians are shown. The fit to the entire distribution, $f(x, E)$, is shown in black.

where x is the measured PSD value. We interpret the fitted Gaussians as likelihood functions:

$$L_\gamma(x; E) = \frac{1}{\sigma_\gamma(E) \sqrt{2\pi}} e^{-\frac{(x-\mu_\gamma(E))^2}{2\sigma_\gamma(E)^2}};$$

$$L_n(x; E) = \frac{1}{\sigma_n(E) \sqrt{2\pi}} e^{-\frac{(x-\mu_n(E))^2}{2\sigma_n(E)^2}}.$$

Because of the weak separation of the distributions, a gamma-pure dataset is used to seed the parameters of the gamma band for the combined gamma/neutron dataset. Figure 6 shows the PSD distribution for an amplitude slice in which the neutron and gamma bands are fairly well separated. The neutron contribution to the distribution is indicated by the red curve, the gamma

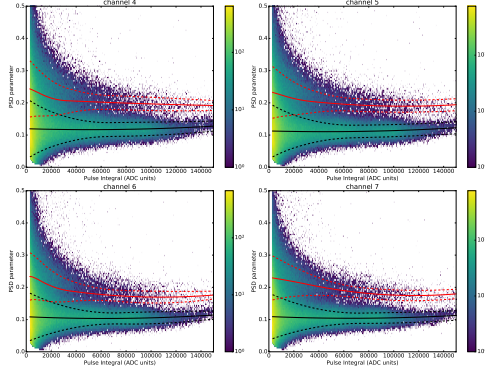


Figure 7: All four PMTs within a cell contribute to the neutron probability defined in Equation 3. The four individual PSD vs. energy distributions for cell 1 are shown here. The mean and 1σ bands are shown for both neutrons (red, and red-dotted) and gammas (black, and black-dotted).

contribution by the green curve, and the total ($f(x, E)$) is the black curve. Figure 7 shows the PSD parameter vs. energy for four PMTs in an individual cell. The resulting mean and standard deviation from the fit slices are shown for both neutron and gamma populations: the neutron mean (μ_n) is indicated by a red solid line, one standard deviation ($\mu_n \pm \sigma_n$) is indicated by red dotted lines, and the gamma mean (μ_γ) and one standard deviation ($\mu_\gamma \pm \sigma_\gamma$) are similarly indicated by black solid and dotted lines.

We then define \hat{P}_n , the Bayesian probability that a given event is a neutron, as

$$\hat{P}_n = \frac{\mathcal{L}_n}{\mathcal{L}_n + R\mathcal{L}_\gamma + \mathcal{L}_o}, \quad (3)$$

where

$$\mathcal{L}_n = \prod_{p=0}^4 \mathcal{L}_n(x_p; p, E_p); \quad \mathcal{L}_\gamma = \prod_{p=0}^4 \mathcal{L}_\gamma(x_p; p, E_p)$$

are the product of the PSD value likelihoods for the individual PMTs, indexed by p . The “other” likelihood value \mathcal{L}_o is a constant factor added to allow for a third category in which the deposition is neither a gamma nor a neutron, such as a pileup event. Finally, the gamma-to-neutron ratio, R , is an energy-dependent factor which is determined for each event. Double Gaussian fits (Eq. (2)) over the PSD parameter distributions are performed on the acquired dataset, fitting for A_n and A_γ , but fixing the μ and σ values to those determined from the calibration dataset. Then for a given event the gamma-to-neutron ratio is taken to be the ratio of the average intensities of the gamma and neutron bands at the four

PMT amplitudes:

$$R = \frac{\sum_p A_{\gamma,p}(E_p)}{\sum_p A_{n,p}(E_p)}. \quad (4)$$

It should be noted that Equation 3 defines a correct probability only under the conditions that the likelihoods are correctly represented by Gaussian distributions at all energies, that the values are independent and identically distributed, that the “other” category is energy-independent and the value is correct, and finally that there are no other distributions contributing. Some of these assumptions are known to be at best approximately true, so $\hat{P}_{n,\gamma}$ are estimates of the correct probabilities.

3.3. Timing

A mismatch between the encoder time (based on the CPU clock) and the digitizer timestamps would result in an offset in the reconstructed source position compared to the true location. To avoid this, the encoder clock and digitizer are synced at the beginning of a run. However, there remains a possibility of a drift in clocks over time, which can also result in positional alignment errors. Significant drift over a data run would cause phase shifts between rotations tending to flatten the counts vs. rotation angle distribution. This is not observed, so any drift between the clocks is small.

4. Analysis

Before source localization, all data is preprocessed. In the preprocessing step a pulse shape parameter is extracted, and then used to estimate the probability that each event is a neutron interaction based on the calibrations described above. We require the \hat{P}_n as defined in Equation 3 to be greater than 0.999 in order to be categorized as a neutron. Each neutron event is then time-sorted and matched to a rotation angle based on the timestamp of the event and a time-tagged list of encoder positions. The result of the preprocessing step is four arrays (or histograms) of neutron counts vs. rotation angle, one for each detector. This is corrected for the detector live time as a function of rotation angle. This correction is necessary due to uneven amounts of time spent accelerating.

Source detection and localization relies on calculating the likelihood of observing a given dataset, both for a background-only hypothesis and for a source-plus-background hypothesis. In this work, a simple isotropic background model is used. For the source model, we assume the signal comes from a single point source with

a fission energy spectrum; since the location and source strength cannot be known in advance, this is necessarily a composite model. We contend that for most source search scenarios, a single-source model is appropriate. If needed, however, both the signal and background models could incorporate added complexity, including additional nuisance parameters representing model unknowns.

Recall from Fig. 1 that ζ is the rotational angle of the detector platform. An isotropic background model predicts an equal probability for background events to be detected in each angle bin, resulting in a constant background probability density function (pdf) $B(\zeta)$. We bin the ζ space into N_b bins, so the normalized pdf is:

$$B_d(\zeta) = 1/N_b. \quad (5)$$

The subscript d indicates detector cell number, although for this background model the four cells have identical pdfs.

The signal pdfs for each detector, $\Xi_d(\zeta; \phi)$, where ϕ is the azimuthal angle of the source location, are experimentally determined from a background-subtracted high-statistics measurement of a single strong neutron source positioned approximately 10 m away. The measured templates are shown in Fig. 8, top. For reference, we also show the equivalent templates for a gamma selection (Fig. 8, bottom), which demonstrate less modulation as expected since this system was designed for neutron sensitivity. This measurement yields $\Xi_d(\zeta; \phi=\phi_0)$ for each of the four detectors, which is then phase-shifted through all possible source locations to determine the pdf for any ϕ .

Next we construct the expected number of counts λ in angle bin ζ , given a source at location ϕ . Since no *a priori* constraints on the signal strength or background rate are assumed, we introduce the signal fraction f_s and consider values in $0 \leq f_s \leq 1$. The expected signal and background contributions are then calculated from N_d , the total number of events observed in cell d , yielding

$$\lambda_d(\zeta, \phi, f_s) = N_d [f_s \Xi_d(\zeta; \phi) + (1 - f_s) B_d(\zeta)]. \quad (6)$$

Finally, we can write the overall likelihood for a given dataset. The background-only likelihood is determined by setting $f_s = 0$. The measured data is represented by the number of events observed in each angle bin for each detector cell, $n_d(\zeta)$. (Note that $N_d = \sum_{\zeta} n_d(\zeta)$.) The likelihood is taken to be the product of Poisson probabilities calculated for each bin; in practice we calculate the log-likelihood:

$$\log \mathcal{L}(\phi, f_s) = \sum_d \sum_{\zeta} \log \left(\frac{e^{-\lambda_d(\zeta)} \lambda_d(\zeta)^{n_d(\zeta)}}{n_d(\zeta)!} \right). \quad (7)$$

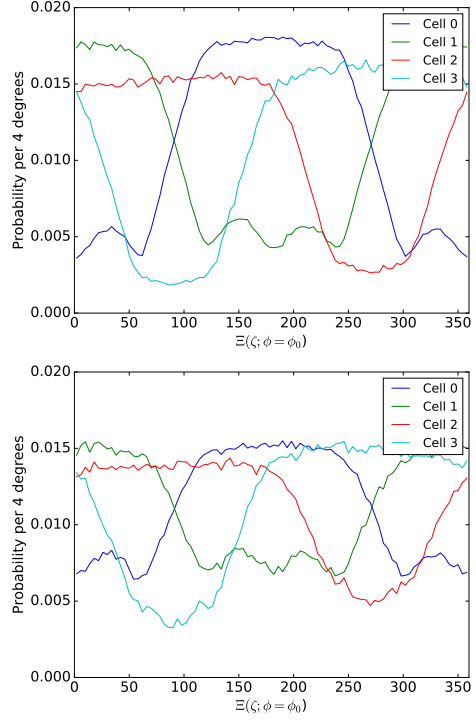


Figure 8: The normalized and background subtracted neutron (top) and gamma (bottom) templates, i.e. $\Xi_d(\zeta; \phi=\phi_0)$.

To illustrate a typical result, Fig. 9 shows the likelihood as a function of ϕ and f_s , with a black line indicating the f_s corresponding to the maximum likelihood for each ϕ . The data were taken from a 24 hour measurement of a 21 μCi ^{252}Cf source at 10 m standoff. For this example, the overall maximum log-likelihood is at $(\phi, f_s) = (0, 0.5)$. For $\sim 90 < \phi < \sim 270$, the maximum log-likelihood is at $f_s = 0$, indicating that the background-only model is preferred over a source located at any of those angles.

Using this log-likelihood, source detection is performed by constructing the test statistic D , the maximum log likelihood ratio between the source-plus-background and background-only hypotheses. The maximum is over all possible source locations, ϕ from 0° to 360° in 90 steps, and over all source strengths, f_s from 0 to 1 in 1000 steps:

$$D = \max_{\phi, f_s} \left[-2 \log \frac{\mathcal{L}(\phi, 0)}{\mathcal{L}(\phi, f_s)} \right]. \quad (8)$$

The test statistic D is then compared to a threshold to determine the presence of a source. The threshold value to be used depends on the measurement time and the desired tradeoff between source detection efficiency and false alarm rate.

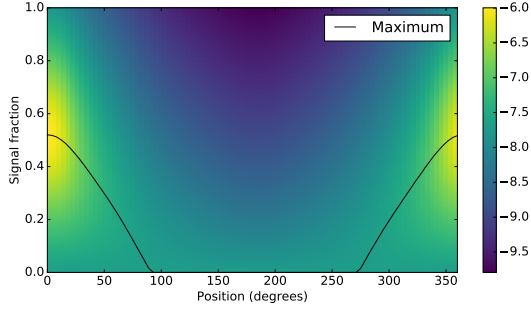


Figure 9: The likelihood as a function of signal fraction f_s and source position ϕ . The z (color) axis is $-\log(-\log \mathcal{L})$, to make the behavior away from the maximum more visible. The f_s corresponding to the maximum likelihood at each source position is indicated by a solid black line. In this example, the overall maximum likelihood is at $(\phi, f_s) = (0, 0.5)$.

Finally, for source localization we use $D(\phi)$, the log likelihood ratio maximized over f_s for a given ϕ :

$$D(\phi) = \max_{f_s} \left[-2 \log \frac{\mathcal{L}(\phi, 0)}{\mathcal{L}(\phi, f_s)} \right]. \quad (9)$$

Then the best estimate for the location of a putative source is $\hat{\phi} = \arg \max_{\phi} D(\phi)$.

5. Measurements and Results

The measurements were taken with the 1D-TEI instrument kept at a stationary location and the source placed at increasing standoff locations of 20 m, 40 m, and 100 m. The instrument was positioned inside a building and next to a large roll-up door. A ^{252}Cf source was placed inside a plastic container sitting on a metal table, with the source located 17 in off the ground. The activity of the ^{252}Cf source was 1.03 mCi, known to 30%, which corresponds to $4.4 \pm 1.3 \times 10^6$ neutrons/s. A picture of the ^{252}Cf source located at 100 m standoff from the instrument is shown in Fig. 10.

We acquired 10 min of data for a 20 m standoff, 1 h for 40 m, 4 h for 100 m, and 47 h with no source present as a background dataset. Care was taken to ensure that there was a clear line of sight between the source and the detector in order to minimize the effects of small-angle scatter. During these measurements, there was a malfunction in detector #2, one of the detectors on the short axis of the diamond; this detector was removed from the analysis, so all results below represent a three-detector system. Data from the three working detectors for the 40 m standoff run is shown in Fig. 11 after the preprocessing analysis stage. For comparison, the data from a background run is shown in Fig. 12.

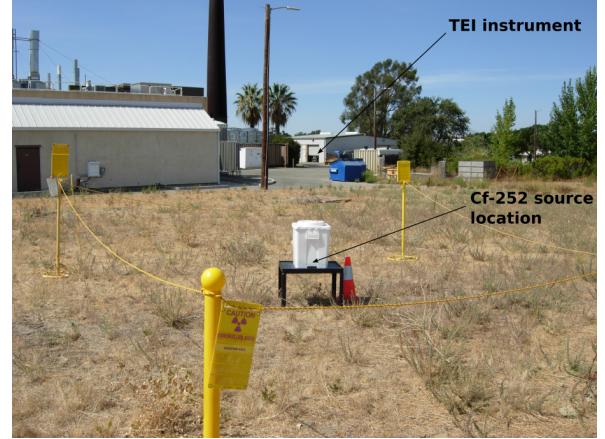


Figure 10: Photo of the ^{252}Cf source placed in a field at 100 m standoff from the detector.

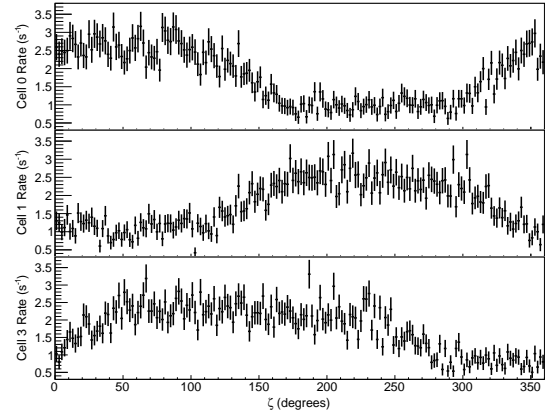


Figure 11: Data for three working detector cells is shown for the 40 m standoff run. Each plot shows the detected neutron rate in 2° bins of system rotation angle ζ for one of the cells.

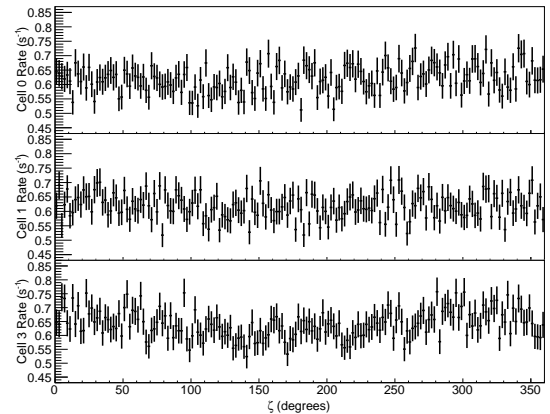


Figure 12: Data for three working detector cells is shown for the background run. Each plot shows the detected neutron rate in 2° bins of system rotation angle ζ for one of the cells.

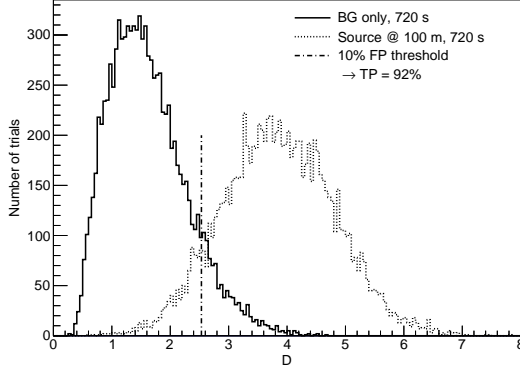


Figure 13: Histograms of the D test statistic distribution for events sampled from the background (solid) and 100 m signal (dotted) datasets. The number of events corresponds to a 720 s measurement, which is the t_d determined for 100 m. A line is drawn at the D threshold that corresponds to a 10% false positive rate as determined from the background-only distribution.

We calculate the test statistic D according to Equation 8. For each standoff distance, we determine the dwell time that gives a 90% detection efficiency with 10% false positives. This required time is denoted t_d in order to distinguish it from the total run time t_r , and is determined as follows. For each distance, we scan over a range of times t and for each t build a D distribution for the signal and background datasets. If N events are observed in the given dataset, $(t/t_r) \cdot N$ events are sampled with replacement and used to calculate D . After repeating this sampling many times, a D distribution is obtained. The background D distribution is used to set a 10% false positive threshold (i.e. at the 90th percentile of the distribution); and the signal D distribution is used to calculate the source detection efficiency ϵ for this threshold. The smallest time t for which $\epsilon > 90\%$ is taken as t_d . For the 100 m dataset, Fig. 13 shows the background and signal D distributions for 10,000 sampled datasets at $t = t_d = 720$ s.

The time t_d is plotted against standoff distance r in Fig. 14; also plotted is a fit to a power law ($t_d = p_0 r^{p_1}$), which yields an exponential power of 4.2. Indeed, $t_d \propto r^4$ is expected behavior from analysis on the simple case of significance in a counting experiment: $S = N_S / \sqrt{N_B}$, where N_S and N_B are the number of signal and background counts, respectively. Since both N_S and N_B scale with acquisition time t , we see that $S \propto \sqrt{t}$. Changing the distance to the source affects the flux at the detector via $1/r^2$, which directly affects the significance, $S \propto 1/r^2$. Thus we see that to maintain a constant significance S under changes in r , we need $t \propto r^4$.

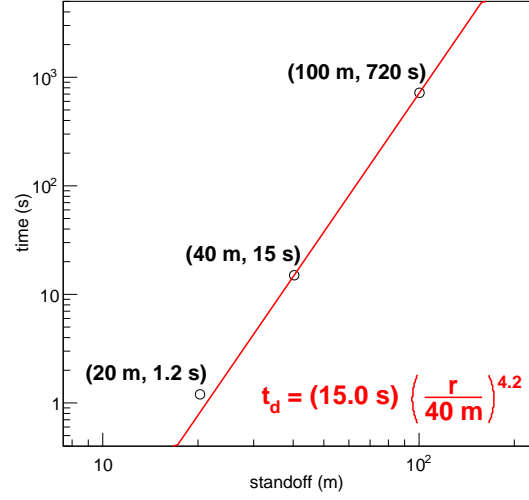


Figure 14: The time t_d yielding 90% efficiency and 10% false positives as a function of standoff distance r for measurements using a 1.03 mCi ($\pm 30\%$) ^{252}Cf source. The power law function fit result is shown in red.

To evaluate the localization resolution of the system, we sample with replacement as described above to create 10,000 resampled datasets for each source standoff distance and for the background-only dataset. We use $t = 720$ s, i.e. t_d as determined for the 100 m source standoff. In Fig. 15, we plot the distributions of $\hat{\phi}$, the estimated source azimuthal angle, for each ensemble of resampled datasets. The true source location for the runs with source present is not precisely known (and is not necessarily identical for the three standoff distances), so we do not evaluate a bias in the estimated direction. The RMS of the $\hat{\phi}$ distribution is 1.6° , 2.5° , and 19° for 20 m, 40 m, and 100 m standoff, respectively, providing an estimate of the system's angular resolution as a function of number of signal events and S:B ratio. We observe some non-uniformity in the background-only dataset. It peaks in the opposite direction from the source position in the field, which may indicate that the non-uniformity is due to neutron production (i.e. the “ship effect”) on large equipment in the building. Note that the likely effect of this particular background non-uniformity on the runs with source present is to reduce the significance of the rate modulation and increase t_d .

The analyzed results for t_d and $\hat{\phi}$ RMS are summarized in Table 1, along with the measured neutron rates and inferred S:B for each run.

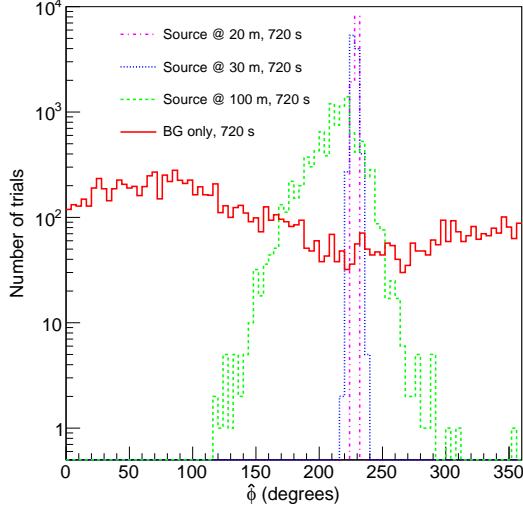


Figure 15: The localization performance is evaluated by plotting $\hat{\phi}$, the estimated source azimuthal angle, for ensembles of resampled datasets corresponding to $t = 720$ s. The true source location for the runs with source present is not precisely known and is not necessarily identical for the three standoff distances, however the peak of each distribution is approximately located in the expected position.

Table 1: Summary of conditions and results for the data runs presented in this article. The signal-to-background ratio S:B is estimated using the measured rates. See text for details on other quantities.

Standoff distance (m)	Overall rate (s^{-1})	S:B	t_d (s)	$\hat{\phi}$ RMS (deg)
20	25.2	12	1.2	1.6
40	5.3	1.8	15	2.5
100	2.1	0.14	720	19
BG	1.9	N/A	N/A	N/A

6. Conclusions

We have presented the design, characterization, and results for a prototype radiological search system. We have demonstrated the ability to detect a ~ 1 mCi ^{252}Cf radiological source at 100 m stand off with 90% detection efficiency and 10% false positives against background in 12 min. This same detection efficiency is met at 15 s for a 40 m standoff, and 1.2 s for a 20 m standoff.

Acknowledgments

Sandia National Laboratories is a multimission laboratory managed and operated by National Technology and Engineering Solutions of Sandia, LLC, a wholly owned subsidiary of Honeywell International, Inc., for the U.S. Department of Energy’s National Nuclear Security Administration under contract DE-NA0003525.

This material is based upon work supported by the U.S. Department of Homeland Security under Grant Award Number, 2012-DN-130-NF0001. The views and conclusions contained in this document are those of the authors and should not be interpreted as representing the official policies, either expressed or implied, of the U.S. Department of Homeland Security.

We would like to thank the US DOE National Nuclear Security Administration, Office of Defense Nuclear Non-proliferation for funding this work.

References

- [1] J. Davis. “Liquid Scintillator Detectors for Fast Neutron Background Characterization with the Radiological Multi-sensor Analysis Platform (RadMAP).” Master’s thesis, University of California at Berkeley, 2015.
- [2] J. Davis, E. Brubaker, and K. Vetter. *Nucl. Inst. and Meth. in Phys. Res. A* **858** (2017) 106-112, doi:10.1016/j.nima.2017.03.042, arXiv:1611.04996.
- [3] J. F. Ziegler. *IBM J. Res. Develop.* **40** (1996) 19-39
- [4] J. E. M. Goldsmith, M.D. Gerling and J. S. Brennan Review of Scientific Instruments **87** (2016) 093307
- [5] P.A. Hausladen, M. A. Blackston, E. Brubaker, D.L. Chichester, P. Marleau, and R.J. Newby. *53rd Annual Meeting of the INMM, Orlando, FL* (2012)
- [6] J. Brennan, E. Brubaker, M. Gerling, K. McMillan, N. Renard-Le Galloudec, M. Sweany. *Nucl. Inst. and Meth. in Phys. Res. A* **802** (2015) 76-81
- [7] A. Nowack, J. Brennan, E. Brubaker, M. Gerling, P. Marleau, K. McMillan, P. Schuster, J. Steele *53rd INMM Annual Meeting* (2012) Orlando, FL.
- [8] J. Brennan, E. Brubaker, M. Gerling, P. Marleau, A. Nowack, P. Shuster. *Proc. SPIE 8852, Hard X-Ray, Gamma-Ray, and Neutron Detector Physics XV* **885203** (September 26, 2013); doi:10.1117/12.2027674
- [9] M. Monterial, P. Marleau, S. Clarke, and S. Pozzi. *Nucl. Inst. and Meth. in Phys. Res. A* **795** 318-324